Special Issue Article

JSA

J Strain Analysis
1–14

DOI: 10.1177/0309324715611524
sdj.sagepub.com
SAGE

Two-dimensional indentation of microstructured solids characterized by couple-stress elasticity

Panos Gourgiotis[1] and Thanasis Zisis[2]

Abstract

In this study, we derive general solutions for two-dimensional plane strain contact problems within the framework of the generalized continuum theory of couple-stress elasticity. This theory introduces characteristic material lengths and is able to capture the associated scale effects that emerge from the material microstructure which are often observed in indentation tests used for the material characterization. The contact problems are formulated in terms of singular integral equations using a Green's function approach. The pertinent Green's function obtained through the use of integral transforms corresponds to the solution of the two-dimensional Flamant–Boussinesq half-plane problem in couple-stress elasticity. The results show a strong dependence on the microstructural characteristics of the material when this becomes comparable to the characteristic dimension of the problem, which in the case of an indentation test is the contact length/area.

Keywords

Contact, Cosserat, Green's function, integral equations, micromechanics, cylindrical indentor, wedge indentor

Date received: 12 July 2015; accepted: 17 September 2015

Introduction

It is well-known that the material microstructure influences the macroscopical behavior of complex materials, such as composites, ceramics, and cellular solids either natural (e.g. wood and cancellous bone) or man-made (e.g. metal or polymer honeycombs and foams). The mechanical properties of cellular materials, for example, depend on the properties of the parent materials that they are made of, on their relative density, and on the cell topology. In such microstructured material, the individual response to a load differs significantly from one cell to another and the assumption that the material's properties are uniformly distributed throughout its volume fails. In addition, the classical continuum theories lose their accuracy when the characteristic wavelength of loading is comparable to the cell size. This consequence of the microstructure upon the macroscopic mechanical response of the materials is usually referred to as "size effect."

Size effects have been observed, among other loading conditions, in indentation tests especially when the indentation characteristic length—that is, the contact width or more commonly the contact area—is comparable to the material microstructure. In particular, it has been shown that a strong size effect emerges upon the hardness in polycrystalline, cellular, and polymer materials especially in the sub-micrometer depth regime. For example, it has been observed that the measured indentation hardness of metals and ceramics increases by a factor of 2 as the width of the indent is decreased from 10 to 1 μm.[1–3] Moreover, indentation of thin films showed an increase in the yield stress with decreasing film thickness.[4] Fleck et al.[5] suggested that the size effect on hardness is related to the high stress/strain gradients present in shallow indentations. In light of the above, and taking into account that the indentation technique has evolved to a standard method for material characterization, the investigation of microstructural effects on the macroscopical behavior of the indented material is significant.[6,7]

[1]Department of Civil, Environmental and Mechanical Engineering, University of Trento, Trento, Italy
[2]Mechanics Division, National Technical University of Athens, Athens, Greece

Corresponding author:
Panos Gourgiotis, Department of Civil, Environmental and Mechanical Engineering, University of Trento, Trento I–38123, Italy.
Email: p.gourgiotis@unitn.it

In general, hardening of the materials is due to combined presence of geometrically necessary dislocations associated with plastic strain gradients and statistically stored dislocations associated with plastic strains. Although strain gradients are extensively used for the interpretation of the size effects in plastic deformation, they are also important for the materials that deform elastically when the representative length of the deformation field becomes comparable to the characteristic lengths of the material microstructure. For example, there are polymers that exhibit significant size effects in the elastic regime.[8,9] In addition, Maranganti and Sharma[10] showed that gradient effects are expected to play a significant role in the elastic deformation of complex cellular type of materials with coarse-grain structure.

During indentation experiments, at very small indentation depth, plastic flow does not occur until the equivalent strain reaches a critical yield value while the recovery during unloading is mainly elastic. For this reason, the elastic contact theory is generally used in order to determine the elastic modulus from a simple analysis of the indentation load–displacement data.[11] Under such circumstances, the observed response of the material may be interpreted only through elasticity considerations and strain gradients may play a significant role upon the macroscopic response.

In order to study the size effects of microstructured materials upon various loading conditions, two different paths may be followed. The first one consists of taking into account the distinct morphology of the material through discrete modeling and incorporating the details of the material microstructure. This approach although very detailed and accurate suffers since the computational cost becomes increasingly high with increasing material complexity. The alternative is the use of a generalized continuum theory according to which the microstructural characteristics are smeared out, but the characteristic microstructural length is retained. The generalized continuum approach is very powerful since it can be incorporated efficiently into large computations but of course lacks the detailed description of a discrete representation and treats the microstructural length in an average sense. Discrete modeling of the material microstructure during indentation has been carried out using classical theories,[3,12–16] whereas phenomenological approaches based on generalized continua have also been extensively followed.[17–22]

One of the most effective generalized continuum theories is the so-called couple-stress elasticity—also known as Cosserat theory with constrained rotations.[23–25] This theory is the simplest gradient theory in which couple-stresses make their appearance. The couple-stress theory may be viewed as a generalization of classical elasticity theory and differs from the classical theory in several significant respects. In particular, the modified strain-energy density and the resulting constitutive relationships involve besides the usual infinitesimal strains and gradients of the rotation vector. Also, the generalized stress–strain relationships for the isotropic case include, in addition to the conventional pair of elastic constants, two new elastic constants, one of which is expressible in terms of a material parameter ℓ that has dimension of length.

The couple-stress theory had some successful applications, mainly on stress concentration problems, in the 1960s and 1970s. However, in recent years, there is a renewed interest in couple-stress theory and related gradient theories dealing with problems of microstructured materials concerning fracture, plasticity, dislocations, and wave propagation. Recent applications include work by, among others, Fleck et al.,[5] Vardoulakis and Sulem,[26] Huang et al.,[27] Lubarda and Markenscoff,[28] Fleck and Hutchinson,[29] Georgiadis and Velgaki,[30] Grammenoudis and Tsakmakis,[31] Grentzelou and Georgiadis,[32] Radi,[33] Gourgiotis and Georgiadis,[34] Dal Corso and Willis,[35] Gourgiotis and Piccolroaz,[36] Triantafyllou and Giannakopoulos,[37] and Zisis et al.[38]

The physical relevance of the material length scales as introduced through generalized continuum theories has been the subject of numerous theoretical and experimental studies. Chen et al.[39] developed a continuum model for cellular materials and concluded that the continuum description of these materials obeys a gradient elasticity theory of the couple-stress type. In the latter study, the intrinsic material length was naturally identified with the cell size. Furthermore, regarding cellular solids, Tekoglu and Onck[16] compared the analytical results of various gradient-type generalized continuum theories with the computational results of discrete models through a range of basic boundary value problems based on Voronoi representations of cellular microstructures. The analysis that was performed strictly within the elastic regime assessed the capabilities of generalized continuum theories in capturing size effects in cellular solids and connected the cell size with the microstructural length scale. Additionally, a recent study by Bigoni and Drugan[40] provided an account of the determination of the couple-stress moduli via homogenization of heterogeneous materials. Moreover, Shodja et al.[41] utilizing ab initio density functional theory (DFT) calculations evaluated the characteristic material lengths of the gradient elasticity theory for several face-centered cubic (FCC) and body-centered cubic (BCC) metal crystals.

Experiments with phonon dispersion curves indicate that for most metals, the characteristic internal length is of the order of the lattice parameter, about 0.25 nm (Zhang and Sharma[42]) while other small-molecule materials have larger internal characteristic lengths. For example, for the semiconductor gallium arsenide (GaAs), Zhang and Sharma[43] estimated a characteristic length of about 0.82 nm, while Lakes[44] estimated a microstructural length for graphite H257 of the order of 2.8 nm. On the other hand, in foams and cellular materials, the characteristic lengths are comparable to

the average cell size, whereas in laminates it is of the order of the laminate thickness. For example, dense polyurethane foams exhibit a microstructural length about 0.33 mm (Lakes[45]), while for human bones it is around 0.5 mm (Lakes[44]).

In this article, we deal with two characteristic plane strain contact problems in couple-stress elasticity, namely, the indentation of a half-plane by a cylindrical and a wedge indentor. It is noted that Muki and Sternberg[17] were the first to study the effects of couple-stresses upon the flat-punch indentation response employing the method of dual integral equations. More recently, Zisis et al.[38] studied some classical two-dimensional (2D) contact problems in the context of couple-stress elasticity using the technique of integral transforms and generalized functions. Here, a more general approach is followed based on the derivation of the fundamental Green's function which corresponds to the solution of the 2D Flamant–Boussinesq half-plane problem in couple-stress elasticity.

The article is structured as follows: initially, we present the fundamental aspects of couple-stress elasticity under plane strain conditions. The half-plane Green's function is then derived using an integral transform analysis. Employing next the pertinent Green's function, the contact problems of a cylindrical and a wedge indentor are formulated in terms of integral equations which are solved by analytical considerations on singular integrals and a numerical treatment using the collocation method. The results for the two different indentation methods are presented and the influence of the microstructure on the solution is discussed in detail. Finally, we consider the inverse problem of practical importance which corresponds to the determination of the punch profile for a given traction distribution over the surface of the half-plane.

Basic equations in plane strain

In this section, we recall briefly certain pertinent elements of the linearized plane strain theory of couple-stress elasticity for homogeneous and isotropic elastic solids. Detailed presentations of the couple-stress theory can be found in the fundamental articles of Mindlin and Tiersten[23] and Koiter.[25] An interesting exposition of the theory under plane strain conditions was given in the work by Muki and Sternberg[17] for the quasi-static case, and more recently by Gourgiotis and Piccolroaz[36] for the dynamical case.

In Figure 1, the rectangular components of the asymmetric stress $(\sigma_{xx}, \sigma_{xy}, \sigma_{yx}, \sigma_{yy})$ and couple-stress (m_{xz}, m_{yz}) are shown, which act upon the faces of an infinitesimal rectangular element of unit thickness. If the stresses and couple-stresses vary across the element, the shear stresses $(\sigma_{xy}, \sigma_{yx})$ are not necessarily equal, and if the shear stresses are equal or even zero, the couple-stresses need not vanish.

For a body that occupies a domain in the (x, y)-plane under conditions of plane strain, the displacement field takes the general form

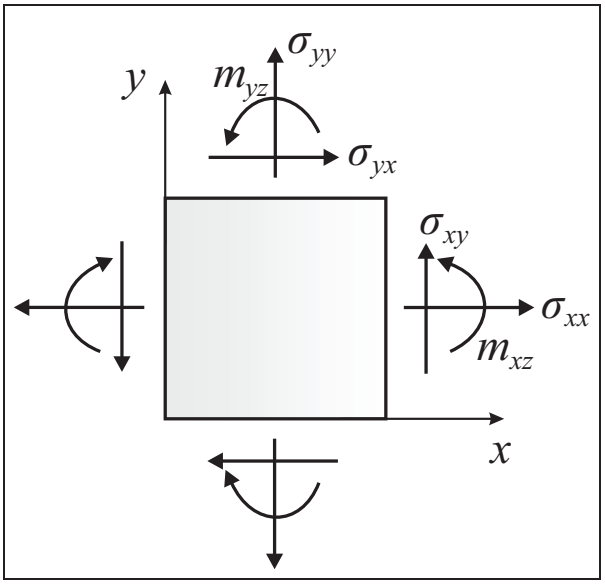

Figure 1. Rectangular components of stress and couple-stress.

$$u_x \equiv u_x(x, y) \neq 0, \quad u_y \equiv u_y(x, y) \neq 0, \quad u_z \equiv 0 \tag{1}$$

Furthermore, for the kinematical description, the following quantities are defined in the framework of the geometrically linear theory

$$\epsilon_{xx} = \frac{\partial u_x}{\partial x}, \quad \epsilon_{yy} = \frac{\partial u_y}{\partial y}, \quad \epsilon_{xy} = \epsilon_{yx} = \frac{1}{2}\left(\frac{\partial u_y}{\partial x} + \frac{\partial u_x}{\partial y}\right) \tag{2}$$

$$\omega = \frac{1}{2}\left(\frac{\partial u_y}{\partial x} - \frac{\partial u_x}{\partial y}\right), \quad \kappa_{xz} = \frac{\partial \omega}{\partial x}, \quad \kappa_{yz} = \frac{\partial \omega}{\partial y} \tag{3}$$

where $\boldsymbol{\epsilon}$ is the usual strain tensor, ω is the rotation, and $(\kappa_{xz}, \kappa_{yz})$ are the non-vanishing components of the curvature tensor (i.e. the gradient of rotation) expressed in dimensions of $[\text{length}]^{-1}$.

Accordingly, assuming vanishing body forces and body couples, the equations of equilibrium in the present circumstances reduce to

$$\begin{aligned} &\frac{\partial \sigma_{xx}}{\partial x} + \frac{\partial \sigma_{yx}}{\partial y} = 0, \quad \frac{\partial \sigma_{xy}}{\partial x} + \frac{\partial \sigma_{yy}}{\partial y} = 0, \\ &\sigma_{xy} - \sigma_{yx} + \frac{\partial m_{xz}}{\partial x} + \frac{\partial m_{yz}}{\partial y} = 0 \end{aligned} \tag{4}$$

Equations (4) are the Cosserat equations of equilibrium in two dimensions. Moreover, the constitutive equations read

$$\begin{aligned} \varepsilon_{xx} &= (2\mu)^{-1}\left[\sigma_{xx} - \nu(\sigma_{xx} + \sigma_{yy})\right], \\ \varepsilon_{yy} &= (2\mu)^{-1}\left[\sigma_{yy} - \nu(\sigma_{xx} + \sigma_{yy})\right], \\ \varepsilon_{xy} &= (4\mu)^{-1}(\sigma_{xy} + \sigma_{yx}) \end{aligned} \tag{5}$$

and

$$\kappa_{xz} = (4\mu\ell^2)^{-1} m_{xz}, \quad \kappa_{yz} = (4\mu\ell^2)^{-1} m_{yz} \tag{6}$$

where μ, ν, and ℓ stand, respectively, for the shear modulus, Poisson's ratio, and the characteristic material length of couple-stress theory.[24]

The compatibility equations in terms of the stress and the couple-stress components assume then the following form[17]

$$\frac{\partial^2\sigma_{xx}}{\partial y^2}-\frac{\partial^2}{\partial x\partial y}(\sigma_{xy}+\sigma_{yx})+\frac{\partial^2\sigma_{yy}}{\partial x^2}=\nu\nabla^2(\sigma_{xx}+\sigma_{yy}) \tag{7}$$

$$\frac{\partial m_{xz}}{\partial y}=\frac{\partial m_{yz}}{\partial x} \tag{8}$$

$$m_{xz}=-2\ell^2\frac{\partial}{\partial y}\left[\sigma_{xx}-\nu(\sigma_{xx}+\sigma_{yy})\right]+\ell^2\frac{\partial}{\partial x}(\sigma_{xy}+\sigma_{yx}) \tag{9}$$

$$m_{yz}=2\ell^2\frac{\partial}{\partial x}\left[\sigma_{yy}-\nu(\sigma_{xx}+\sigma_{yy})\right]-\ell^2\frac{\partial}{\partial y}(\sigma_{xy}+\sigma_{yx}) \tag{10}$$

Note that only three of the four equations of compatibility are independent. Indeed, equations (8)–(10) imply equation (7), while equations (7), (9), and (10) yield equation (8).[17,24]

The complete solution of equations (4) admits the following representation in terms of the Mindlin's stress functions[24]

$$\sigma_{xx}=\frac{\partial^2\Phi}{\partial y^2}-\frac{\partial^2\Psi}{\partial x\partial y},\quad \sigma_{yy}=\frac{\partial^2\Phi}{\partial x^2}+\frac{\partial^2\Psi}{\partial x\partial y}$$
$$\sigma_{xy}=-\frac{\partial^2\Phi}{\partial x\partial y}-\frac{\partial^2\Psi}{\partial y^2},\quad \sigma_{yx}=-\frac{\partial^2\Phi}{\partial x\partial y}+\frac{\partial^2\Psi}{\partial x^2} \tag{11}$$

and

$$m_{xz}=\frac{\partial\Psi}{\partial x},\quad m_{yz}=\frac{\partial\Psi}{\partial y} \tag{12}$$

where $\Phi\equiv\Phi(x,y)$ and $\Psi\equiv\Psi(x,y)$ are the arbitrary but sufficiently smooth functions. Furthermore, substitution of equations (11) and (12) into equations (9) and (10) results in the following pair of differential equations, for the stress functions

$$\frac{\partial}{\partial x}(\Psi-\ell^2\nabla^2\Psi)=-2(1-\nu)\ell^2\nabla^2\left(\frac{\partial\Phi}{\partial y}\right) \tag{13}$$

$$\frac{\partial}{\partial y}(\Psi-\ell^2\nabla^2\Psi)=2(1-\nu)\ell^2\nabla^2\left(\frac{\partial\Phi}{\partial x}\right) \tag{14}$$

which, accordingly, lead to the uncoupled partial differential equations (PDEs)

$$\nabla^4\Phi=0 \tag{15}$$

$$\nabla^2\Psi-\ell^2\nabla^4\Psi=0 \tag{16}$$

Note that the above representation reduces to the classical Airy's representation as the quantities ℓ, $\partial_x\Psi$, and $\partial_y\Psi$ tend to zero. In addition, combining equations (2)–(5) and (11) and (12), one can obtain the following relations expressing the displacement gradients in terms of Mindlin's stress functions

$$\frac{\partial u_x}{\partial x}=\frac{1}{2\mu}\left(\frac{\partial^2\Phi}{\partial y^2}-\frac{\partial^2\Psi}{\partial x\partial y}-\nu\nabla^2\Phi\right) \tag{17}$$

$$\frac{\partial u_y}{\partial y}=\frac{1}{2\mu}\left(\frac{\partial^2\Phi}{\partial x^2}+\frac{\partial^2\Psi}{\partial x\partial y}-\nu\nabla^2\Phi\right) \tag{18}$$

$$\frac{\partial u_x}{\partial y}+\frac{\partial u_y}{\partial x}=-\frac{1}{2\mu}\left(2\frac{\partial^2\Phi}{\partial x\partial y}-\frac{\partial^2\Psi}{\partial x^2}+\frac{\partial^2\Psi}{\partial y^2}\right) \tag{19}$$

Half-plane Green's functions

The definition of a Green's function can be used mathematically to derive solutions to point load problems, either within the elastic body or on its surface. A multitude of Green's functions within the context of classical elasticity is available in the literature for different surface geometries (see, e.g., Green and Zerna[46]). In a 2D setting, the problem of determining the stress and displacement fields in an isotropic half-space subjected to a concentrated line load on its surface is the celebrated Flamant–Boussinesq problem (see Figure 2). The Flamant–Boussinesq solution of classical elasticity is discussed among others, for example, by Love,[47] Fung,[48] and Timoshenko and Goodier,[49] and enjoys important applications mainly in contact mechanics and tribology, since it can be used as a building block for the formulation of complicated contact problems (see, e.g., Johnson,[50] Hills and Nowell,[51] and Barber[52]).

In the context of generalized continuum theories, concentrated load problems have been extensively studied suggesting solutions that significantly depart from the predictions of classical elasticity. A thorough review on the subject can be found in the recent work of Georgiadis and Anagnostou.[53] Regarding the couple-stress theory, Muki and Sternberg[17] were the first to derive the asymptotic fields for the stress field in the Flamant–Boussinesq problem. Here, we provide a full-field solution for the Flamant–Boussinesq problem which is accordingly used as the pertinent Green's function for the formulation of the plane contact problems.

We consider a body occupying the half-plane $(-\infty<x<\infty, y>0)$ under plane strain conditions subjected to a normal line load P on its surface. The

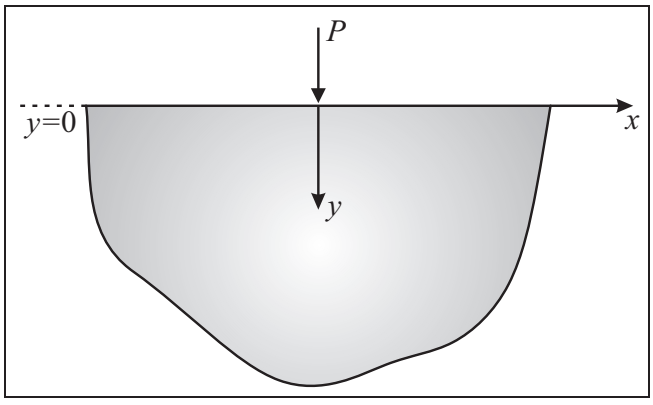

Figure 2. Normal load acting on the surface of an elastic half-plane.

point of application of the concentrated load is taken as the origin ($x = y = 0$) of a Cartesian rectangular coordinate system. The intensities of the concentrated loads are expressed in dimensions of [force] [length]$^{-1}$.

The boundary conditions along the surface $y = 0$ become

$$\sigma_{yy}(x,0) = -P\delta(x) \quad \text{for} \quad -\infty < x < \infty \tag{20}$$

$$\sigma_{yx}(x,0) = 0 \quad \text{for} \quad -\infty < x < \infty \tag{21}$$

$$m_{yz}(x,0) = 0 \quad \text{for} \quad -\infty < x < \infty \tag{22}$$

where $\delta(x)$ is the Dirac delta function. It is noted that the solution procedure for the case of a tangential load acting on the surface of a half-plane is directly analogous to what will be presented next and for this reason is omitted for sake of brevity.

The problem is attacked with the aid of the Fourier transform on the basis of the stress function formulation summarized earlier. The direct Fourier transform and its inverse are defined as follows

$$\hat{f}(\xi) = \int_{-\infty}^{\infty} f(x) e^{i\xi x} dx \tag{23}$$

$$f(x) = \frac{1}{2\pi} \int_{-\infty}^{\infty} \hat{f}(\xi) e^{-i\xi x} d\xi \tag{24}$$

where $i \equiv (-1)^{1/2}$.

The transformation of equations (15) and (16) employing equation (23) yields the following ordinary differential equations (ODEs) for the transformed stress functions

$$\frac{d^4\hat{\Phi}}{dy^4} - 2\xi^2 \frac{d^2\hat{\Phi}}{dy^2} + \xi^4 \hat{\Phi} = 0 \tag{25}$$

$$\ell^2 \frac{d^4\hat{\Psi}}{dy^4} - (1 + 2\ell^2\xi^2) \frac{d^2\hat{\Psi}}{dy^2} + \xi^2(1 + \ell^2\xi^2)\hat{\Psi} = 0 \tag{26}$$

whereas the transformed stresses, couple-stresses, and displacements become

$$\hat{\sigma}_{xx} = \frac{d^2\hat{\Phi}}{dy^2} + i\xi \frac{d\hat{\Psi}}{dy}, \quad \hat{\sigma}_{yy} = -\xi^2\hat{\Phi} - i\xi \frac{d\hat{\Psi}}{dy}$$

$$\hat{\sigma}_{yx} = i\xi \frac{d\hat{\Phi}}{dy} - \xi^2\hat{\Psi}, \quad \hat{\sigma}_{xy} = i\xi \frac{d\hat{\Phi}}{dy} - \frac{d^2\hat{\Psi}}{dy^2} \tag{27}$$

$$\hat{m}_{xz} = -i\xi\hat{\Psi}, \quad \hat{m}_{yz} = \frac{d\hat{\Psi}}{dy} \tag{28}$$

and

$$\hat{u}_x = \frac{1}{2\mu\xi}\left(i(1-\nu)\frac{d^2\hat{\Phi}}{dy^2} - \xi\frac{d\hat{\Psi}}{dy} + i\nu\xi^2\hat{\Phi}\right)$$

$$\hat{u}_y = \frac{1}{2\mu\xi^2}\left((1-\nu)\frac{d^3\hat{\Phi}}{dy^3} - (2-\nu)\xi^2\frac{d\hat{\Phi}}{dy} - i\xi^3\hat{\Psi}\right) \tag{29}$$

The governing equations (25) and (26) have the following bounded solution as $y \to +\infty$

$$\hat{\Phi}(\xi, y) = [C_1(\xi) + yC_2(\xi)]e^{-|\xi|y} \tag{30}$$

$$\hat{\Psi}(\xi, y) = C_3(\xi)e^{-|\xi|y} + C_4(\xi)e^{-\gamma y} \tag{31}$$

where $\gamma \equiv \gamma(\xi) = (1/\ell^2 + \xi^2)^{1/2}$.

Enforcing now the boundary conditions (21) and (22) results in the following equations for the unknown functions $C_i(\xi)$ ($i = 1, \ldots, 4$)

$$C_2(\xi) = |\xi|C_1(\xi) - i\xi(1 - |\xi|^{-1}\gamma)C_4(\xi) \tag{32}$$

$$C_3(\xi) = -\gamma|\xi|^{-1}C_4(\xi) \tag{33}$$

where the functions $C_2(\xi)$ and $C_3(\xi)$ are related through the compatibility equations (13) and (14) as follows

$$C_3(\xi) = -4i\ell^2(1-\nu)\xi C_2(\xi) \tag{34}$$

Upon substitution of the functions $C_i(\xi)$ into equations (29)–(31), and utilizing the fact that $\hat{u}_x(x,\xi)$ and $\hat{u}_y(x,\xi)$ are odd and even functions of ξ, respectively, the components of the transformed displacement field become

$$u_x(x,y) = \frac{-i}{\pi}\int_0^{\infty} \hat{u}_x(\xi, y)\sin(\xi x)d\xi \tag{35}$$

$$u_y(x,y) = \frac{1}{\pi}\int_0^{\infty} \hat{u}_y(\xi, y)\cos(\xi x)d\xi \tag{36}$$

where

$$\hat{u}_x(\xi,y) = \frac{iP}{2\mu\xi\Delta}\left[4\ell^2(1-\nu)\xi^2\gamma e^{-\gamma y} + \left(\gamma(y\xi - 1 + 2\nu) - 4\ell^2(1-\nu)\xi^3\right)e^{-\xi y}\right], \tag{37}$$

$$\hat{u}_y(\xi,y) = \frac{P}{2\mu\xi\Delta}\left[4\ell^2(1-\nu)\xi^3 e^{-\gamma y} + (\gamma(y\xi + 2(1-\nu)) - 4\ell^2(1-\nu)\xi^3)e^{-\xi y}\right], \tag{38}$$

and

$$\Delta \equiv \Delta(\xi) = \gamma - 4(1-\nu)\ell^2\xi^2(\xi - \gamma).$$

The tangential displacement $u_x(x,y)$ can be numerically evaluated due to the fact that $\hat{u}_x(\xi,y)$ is bounded as $\xi \to 0$. On the other hand, the inversion integral (36) is divergent since the integrand behaves as $\hat{u}_y(\xi,y) = O(\xi^{-1})$ for $\xi \to 0$ and, thus, has to be interpreted in the finite part sense (a situation analogous to the classical elasticity case).

It is noted that in classical elasticity, the solutions for the normal and tangential displacements are[52]

$$u_x^{class}(x,y) = \frac{P}{2\pi\mu}\left[\frac{xy}{r^2} - (1-2\nu)\tan^{-1}\left(\frac{x}{y}\right)\right] \tag{39}$$

$$u_y^{class}(x,y) = \frac{P}{2\pi\mu}\left[\frac{y^2}{r^2} - 2(1-\nu)\log(r)\right] \tag{40}$$

The asymptotic behavior of the tangential and normal displacements in the context of couple-stress elasticity is examined now near the point of the application of the concentrated load. To this purpose, we employ theorems of the Abel–Tauber type[54] and examine the behavior of the transformed solutions (37) and (38) as $\xi \to \infty$. In particular, it can be readily shown that

$$u_x^{asympt}(x,y) = \frac{P}{2\mu\pi(3-2\nu)}\left[-(1-2\nu)\frac{xy}{r^2} + \tan^{-1}\left(\frac{x}{y}\right)\right] \tag{41}$$

$$u_y^{asympt}(x,y) = -\frac{P}{2\pi\mu(3-2\nu)}\left[(1-2\nu)\frac{y^2}{r^2} + 2(1-\nu)\log(r)\right], \tag{42}$$

with $r = (x^2 + y^2)^{1/2}$. It is noted that the displacement components exhibit the same asymptotic behavior both in couple-stress and classical elasticity; however, the detailed structure of these fields is different. The strain components can be readily calculated from equations (35) and (36) through appropriate derivations. In fact, it can be shown that the strains remain singular and behave as $\varepsilon_{ij} = O(r^{-1})$ for $r \to 0$. However, in marked contrast to the classical theory, the rotation is bounded at the point of application of the load. It is recalled that in the classical theory, the rotation is singular, exhibiting an $\sim r^{-1}$ variation as $r \to 0$.

Although it is certainly possible to formulate contact problems using equations (35) and (36), it is often more convenient to work in terms of the displacement gradients, thereby eliminating arbitrary constants.[52] To this respect, the quantity du_y/dx is evaluated at the surface of the half-plane ($y = 0$) as

$$\frac{du_y}{dx} = \frac{1}{\pi}\int_0^\infty g(\xi)\sin(\xi x)d\xi \tag{43}$$

with $g(\xi) = -\xi\hat{u}_y(\xi,0)$. The integral in equation (43) is divergent since $g(\xi) = O(1)$ as $\xi \to \infty$. In order to make $g(\xi)$ explicit and separate its singular and regular parts, it is expedient to examine the asymptotic behavior of $g(\xi)$ as $\xi \to \infty$. Using the Abel–Tauber theorem and noting that $\lim_{\xi\to\infty} g(\xi) = g_\infty(\xi) = -(P(1-\nu))/(\mu(3-2\nu))$, we decompose $g(\xi)$ as

$$g(\xi) = g_\infty(\xi) + (g(\xi) - g_\infty(\xi)) \tag{44}$$

Equation (43) then takes the following form

$$\frac{du_y}{dx} = \underbrace{\frac{1}{\pi}\int_0^\infty g_\infty(\xi)\sin(\xi x)d\xi}_{\text{singular part}} + \underbrace{\frac{1}{\pi}\int_0^\infty [g(\xi) - g_\infty(\xi)]\sin(\xi x)d\xi}_{\text{regular part}} \tag{45}$$

which, after utilizing certain results of the theory of the theory generalized functions and singular distributions,[54] equation (45) can be rewritten as

$$\frac{du_y}{dx} = -\frac{P}{\pi\mu}\frac{(1-\nu)}{(3-2\nu)}\frac{1}{x} + \frac{P}{\pi\mu}N(x) \tag{46}$$

where

$$N(x) = \frac{2(1-\nu)^2}{(3-2\nu)}\int_0^\infty \frac{\left(2\ell^2\xi^2(\gamma-\xi)-\gamma\right)}{\gamma + 4(1-\nu)\ell^2\xi^2(\gamma-\xi)}\sin(\xi x)d\xi, \tag{47}$$

Equation (46) will be used next to construct the integral equations for the contact problems.

Before we proceed further, we present some representative results regarding the displacements and the rotation in the Flamant–Boussinesq problem. In Figures 3 and 4, the normal displacement and the rotation are illustrated at the surface of the half-plane ($y = 0$) and inside the half-plane, respectively. The results regarding the quantities at the surface are presented for various Poisson's ratios while contours inside the half-plane are shown only for $\nu = 0.33$. In both figures, the classical elasticity results are overlaid. Regarding the normal displacement, it can be seen that the logarithmically singular response of the classical solution as x/ℓ approaches the point of the application of the load is retained in the couple-stress solution as well. Note that the classical elasticity solution for the present normalization is independent of the Poisson's ratio effect, while the solution of the couple-stress elasticity for the same normalization retains the dependence upon ν. Regarding the rotation, it is noted that the classical elasticity solution suggests an unbounded behavior at the point of the application of the load; however, this singular response is eliminated in the couple-stress elasticity, showing *zero* rotation at the same point. Of course, the effect of the Poisson's ratio in the case of the couple-stress elasticity is apparent in contrast to the classical elasticity case for the present normalization. It is emphasized that the effect of the couple-stresses is significant near the point of the application of the load where the rotation/strain gradients are more pronounced. Indeed, the couple-stress solution approaches the classical one while the effect of the Poisson's ratio disappears as we move further from the loading source.

Formulation of the contact problems

We now consider the stresses produced in an elastic half-plane by the action of a rigid indentor pressed into the surface as shown in Figure 5(a) and (b). A Cartesian coordinate system $Oxyz$ is attached at the center line of the geometry. A load P is applied to the indentor which, in the plane strain case, has dimensions of [force][length]$^{-1}$.

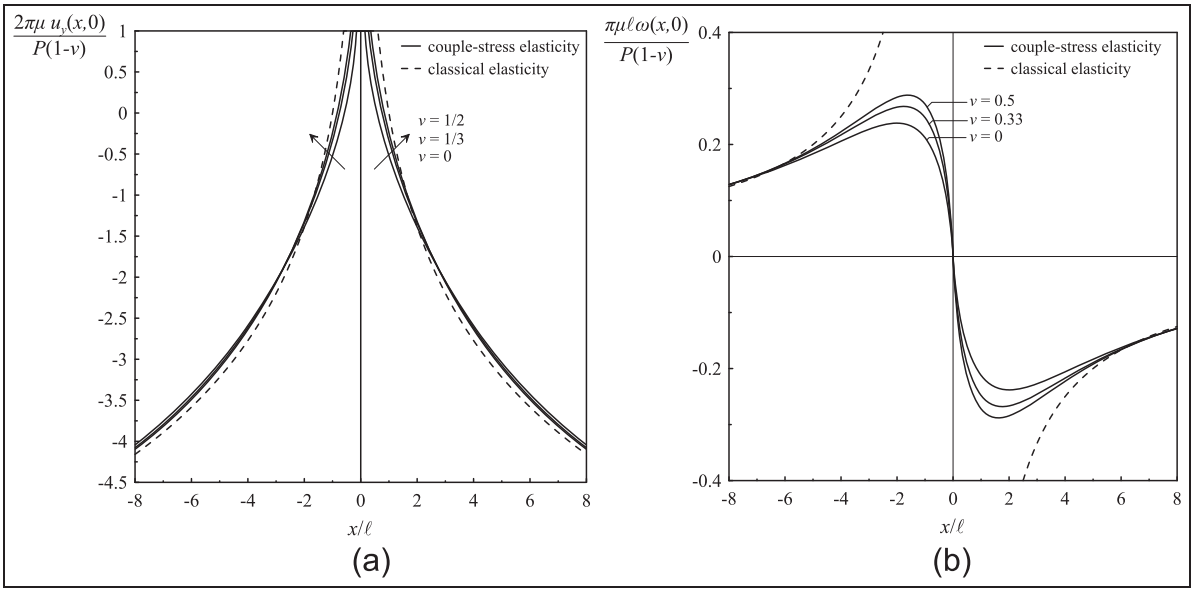

Figure 3. Dimensionless (a) normal displacement and (b) rotation along the surface of the half-plane due to the application of normal point load P. Results are shown for different Poisson's ratios ν.

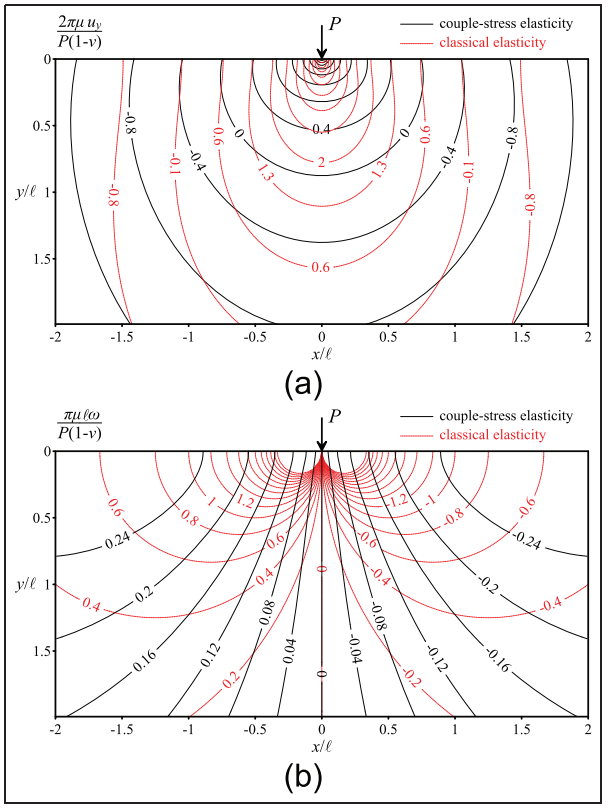

Figure 4. Dimensionless level sets of (a) normal displacement and (b) rotation for the Flamant–Boussinesq problem. For both cases, the Poisson's ratio is $\nu = 0.33$.

We begin by considering the limit of the Hertz elliptical contact where one axis of the ellipse becomes considerably larger than the other axis.[51] This limit corresponds to a cylindrical indentor of radius R with its axis lying parallel to the z-axis in the current coordinate system pressed in contact with a half-plane under the action of the force P. The two bodies are making contact over a long strip of width $2b$ lying parallel to the x-axis (Figure 5(a)). Then, a second solution is given for the pressure below a wedge indentor pressed in contact with an elastic half-plane. In this case, in order for the deformations to be sufficiently small and lie within the frame of the linear theory, the semi-angle α of the wedge must be close to 90° (here $\alpha = 88^\circ$).

For the points lying within the contact area $(-b < x < b)$ after loading, we have the following general geometrical boundary condition

$$u_y = k(x) \tag{48}$$

which, depending on the type of the profile, takes the following two forms

1. $k(x) = \delta - (1/2R)x^2$, for the cylindrical indentor
2. $k(x) = \delta - |x|\cot(\alpha)$, for the wedge indentor

where δ is a positive constant.

Regarding the traction boundary conditions, we note that since no restriction is imposed on u_x and du_x/dy under the indentor, the rotation ω is arbitrary at the contact area. Thus, by enforcing the principle of virtual power,[25] we approximate zero shear and couple tractions under the indentor. In view of the above, the following traction boundary conditions hold for a frictionless and smooth contact[20]

$$\sigma_{yy}(x,0) = 0 \quad \text{for} \quad |x| > b \tag{49}$$

$$\sigma_{yx}(x,0) = 0 \quad \text{for} \quad -\infty < x < \infty \tag{50}$$

$$m_{yz}(x,0) = 0 \quad \text{for} \quad -\infty < x < \infty \tag{51}$$

which are accompanied by the auxiliary condition

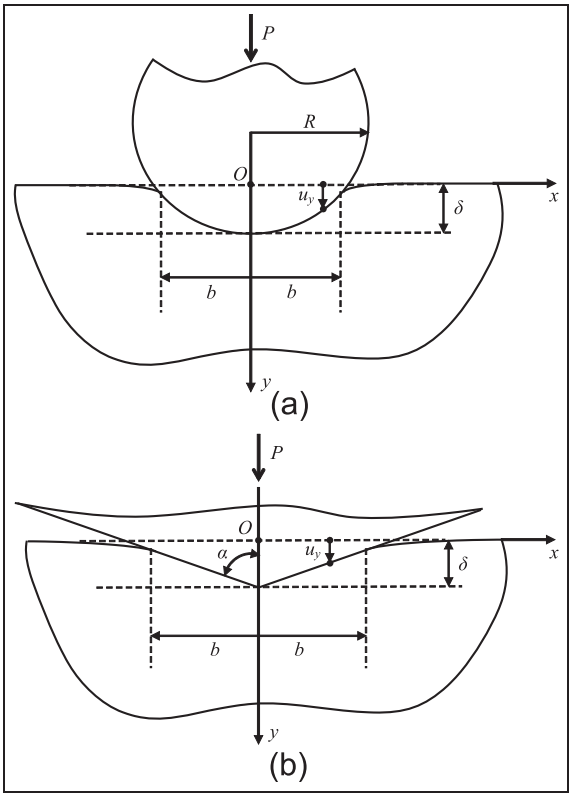

Figure 5. Definition of the problem of (a) a cylindrical rigid body indenting an elastic half-plane and (b) a rigid wedge indenting an elastic half-plane.

$$\int_{-b}^{b} \sigma_{yy}(x,0)dx = -\int_{-b}^{b} p(x)dx = -P \tag{52}$$

where $p(x)$ is the pressure below the indentor with the following properties

$$p(x) = 0 \quad (|x| > b) \quad \text{and} \quad p(x) = p(-x) \quad (|x| < b) \tag{53}$$

Moreover, since the indented surface is an unbounded region, the above boundary conditions must be supplemented by the regularity conditions at infinity

$$\sigma_{ij} \to 0 \quad \text{and} \quad m_{ij} \to 0 \quad \text{as} \quad r \to \infty \tag{54}$$

Singular integral equation approach

Our objective now is the determination of the contact-stress distribution below the rigid indentor and the determination of the associated contact length. Now suppose that the surface of the half-plane is subjected to a distributed normal load $p(\xi)$ per unit length. The stress and displacement fields can be found by superposition using the Flamant–Boussinesq solution as the pertinent Green's function—that is, treating the distributed load as the limit of a set of point loads of magnitude $p(\xi)d\xi$. It should be noted that the Flamant–Boussinesq solution automatically satisfies the traction-free boundary conditions (50) and (51).

In view of the above, the tangential gradient of the normal displacement at the surface of the half-plane assumes the following form

$$\frac{du_y}{dx} = -\frac{(1-\nu)}{(3-2\nu)\pi\mu}\,\mathrm{CPV}\int_{-b}^{b}\frac{p(s)}{x-s}ds + \frac{1}{\pi\mu}\int_{-b}^{b} N(x-s)p(s)ds, \quad |x| < b \tag{55}$$

Accordingly, and taking into account equation (48), we derive, after the appropriate normalization, the governing *singular* integral equation in couple-stress elasticity

$$-\frac{1-\nu}{3-2\nu}\,\mathrm{CPV}\int_{-1}^{1}\frac{p(\tilde{s})}{\tilde{x}-\tilde{s}}d\tilde{s} + \int_{-1}^{1}\tilde{N}(\tilde{x}-\tilde{s})p(\tilde{s})d\tilde{s} = \frac{\pi\mu}{b}\frac{d\tilde{k}(\tilde{x})}{d\tilde{x}}, \quad |\tilde{x}| < 1 \tag{56}$$

with $\tilde{x} = x/b$ and $\tilde{s} = s/b$. Note that the first integral in the integral equation (56) is interpreted in the Cauchy principal value (CPV) sense. In addition, the regular kernel is defined as

$$\tilde{N}(\tilde{x}-\tilde{s}) = \frac{2(1-\nu)^2}{(3-2\nu)} \int_0^{\infty} \frac{2q^2\zeta^2(\tilde{\gamma}-q\zeta)-\tilde{\gamma}}{\tilde{\gamma}+4(1-\nu)q^2\zeta^2(\tilde{\gamma}-q\zeta)}\sin((\tilde{x}-\tilde{s})\zeta)d\zeta, \tag{57}$$

with $\zeta = \xi b$, $q = \ell/b$ and $\tilde{\gamma} = (1+q^2\zeta^2)^{1/2}$. The above convergent integral is a Fourier sine transform and can be efficiently evaluated numerically employing MATHEMATICA™ algorithms that take into account its oscillatory character. It is remarked that the governing integral equation (56) was previously obtained in Zisis et al.[38] employing a different approach based on the method of integral transforms and generalized functions.

Numerical solution and results

The numerical solution of the singular integral equation (56) together with the complementary condition (52) is accomplished by means of the collocation method for each indentor profile.

Indentation by a cylindrical indentor

In classical elasticity, the contact tractions for the cylindrical indentor problem are not singular at the end points of the contact width $x = \pm b$ (Johnson[50]). Accordingly, guided by the results concerning the modification of stress singularities in the presence of couple-

stresses,[34,55] we assume that the pressure distribution assumes the following form

$$p(\tilde{s}) = \sum_{n=0}^{\infty} a_n U_n(\tilde{s})\sqrt{1-\tilde{s}^2} \tag{58}$$

where $U_n(\tilde{s})$ are the Chebyshev polynomials of the second kind. The integral equation then becomes

$$\sum_{n=0}^{\infty} a_n \left\{ -\frac{1-\nu}{3-2\nu}\int_{-1}^{1} \frac{U_n(\tilde{s})\sqrt{1-\tilde{s}^2}}{(\tilde{x}-\tilde{s})} d\tilde{s} + \int_{-1}^{1} U_n(\tilde{s})\sqrt{1-\tilde{s}^2}\tilde{N}(\tilde{x}-\tilde{s})d\tilde{s} \right\} = -\frac{\mu\pi b}{R}\tilde{x}, \quad |\tilde{x}|\leqslant 1 \tag{59}$$

It is remarked that the contact area b is not known a priori and will be determined from the solution of the boundary value problem. In equation (59), the first integral is evaluated as a CPV integral by using the standard relationship

$$\text{CPV}\int_{-1}^{1} \frac{U_n(\tilde{s})\sqrt{1-\tilde{s}^2}}{(\tilde{x}-\tilde{s})} d\tilde{s} = \pi T_{n+1}(\tilde{x}) \quad \text{for} \quad n\geqslant 0, \quad |\tilde{x}|\leqslant 1 \tag{60}$$

Consequently, one reaches to the following functional equation that can be used in the numerical discretization

$$\sum_{n=0}^{\infty} a_n \left\{ -\frac{(1-\nu)\pi}{3-2\nu} T_{n+1}(\tilde{x}) + W_n(\tilde{x}) \right\} = -\frac{\mu\pi b}{R}\tilde{x} \tag{61}$$

where $W_n(\tilde{x}) = \int_{-1}^{1} U_n(\tilde{s})\sqrt{1-\tilde{s}^2}\tilde{N}(\tilde{x}-\tilde{s})d\tilde{s}$ is a regular integral, which can be evaluated by the standard Gaussian quadrature method. Now, equation (61) is solved by truncating the series at $n = N$ and using an appropriate collocation technique with collocation points chosen as the roots of $T_{N+1}(\tilde{x})$, namely, $\tilde{x}_j = \cos((2j-1)\pi/(2(N+1)))$ with $j = 1, 2, \ldots, N+1$. The complementary condition (52) is then used for the evaluation of the unknown contact area $2b$.

Indentation by a wedge indentor

Next, we consider the problem of the sharp wedge indentor. As in the classical theory,[51] we assume that the pressure is non-singular at the end points of the contact area. In this case, the singular integral equation (53) takes the following form

$$-\frac{1-\nu}{3-2\nu}\int_{-1}^{1} \frac{p(\tilde{s})}{\tilde{x}-\tilde{s}} d\tilde{s} + \int_{-1}^{1} \tilde{N}(\tilde{x}-\tilde{s})p(\tilde{s})d\tilde{s}, = -\mu\pi\cot\alpha\,\text{sgn}(\tilde{x}), \quad |\tilde{x}|\leq 1, \tag{62}$$

where sgn( ) is the signum function, and α is the half-angle of the indentor (Figure 5(b)). For the solution of the singular integral equation (62), the approach proposed by Ioakimidis[56] is adopted where the loading function presents jump discontinuities. To this end, we set

$$p(\tilde{x}) = \psi(\tilde{x}) + h(\tilde{x}) \tag{63}$$

where $\psi(\tilde{x})$ is a new function to be determined and $h(\tilde{x})$ satisfies the singular integral equation

$$-\frac{1-\nu}{3-2\nu}\int_{-1}^{1} \frac{h(\tilde{s})}{\tilde{x}-\tilde{s}}\, d\tilde{s} = -\mu\pi\,\text{sgn}(\tilde{x})\cot\alpha, \quad |\tilde{x}|\leqslant 1 \tag{64}$$

Now, equation (66) has the same general form as the integral equation that describes the shallow wedge problem in the classical theory.[50] A closed-form solution is then given by

$$h(\tilde{x}) = \frac{\mu(3-2\nu)\cot\alpha}{\pi(1-\nu)}\log\left(\frac{1+\sqrt{1-\tilde{x}^2}}{1-\sqrt{1-\tilde{x}^2}}\right) \tag{65}$$

Upon substitution of equation (63) into equation (63) and by using equation (64), one arrives at

$$-\frac{1-\nu}{3-2\nu}\int_{-1}^{1} \frac{\psi(\tilde{s})}{\tilde{x}-\tilde{s}}d\tilde{s} + \int_{-1}^{1} \tilde{N}(\tilde{x}-\tilde{s})\psi(\tilde{s})d\tilde{s} = f(\tilde{x}), \quad |\tilde{x}|\leqslant 1 \tag{66}$$

where

$$f(\tilde{x}) = -\int_{-1}^{1} \tilde{N}(\tilde{x}-\tilde{s})h(\tilde{s})d\tilde{s} \tag{67}$$

Furthermore, the complementary condition in equation (54) yields

$$\int_{-1}^{1} \psi(\tilde{x})d\tilde{x} = \frac{P}{b} - \frac{2\mu(3-2\nu)\cot\alpha}{\pi(1-\nu)} \tag{68}$$

It can be readily shown that the function $f(\tilde{x})$ is continuous in the range $\tilde{x}\in[-1, 1]$, and thus, the standard methodology described in the previous section can be directly applied for the solution of equation (68). As in the cylindrical indentor case, we assume that $\psi(\tilde{s})$ has the following form

$$\psi(\tilde{s}) = \sum_{n=0}^{\infty} c_n U_n(\tilde{s})\sqrt{1-\tilde{s}^2} \tag{69}$$

Thus, omitting the details of the analysis, the final functional form of the integral equation becomes

$$\sum_{n=0}^{N} c_n \left\{ -\frac{(1-\nu)\pi}{3-2\nu} T_{n+1}(\tilde{x}) + W_n(\tilde{x}) \right\} = f(\tilde{x}) \qquad (70)$$

Again, the unknown contact length b will be determined from the solution of equation (70) together with the complementary condition (52). The functional equation is solved by employing the same collocation scheme as in previous section. In this case, the solution presented a slower convergence compared to the previous case.

Indentation by a punch generating uniform pressure

A problem of practical interest is the determination of the punch profile for a given traction distribution over the surface of the half-plane. This is an inverse problem compared with those already examined as we are stipulating the pressure distribution and wish to deduce the proper profile of the punch $k(x)$. If the desired contact pressure is constant, $p(x) = p_0$, and contact is made over a strip of width $2b$, the pressure is given by $p_0 = P/2b$, and hence equation (56) is now simply an integral rather than an integral equation. In particular, we obtain

$$\frac{\pi\mu}{bp_0}\frac{d\tilde{k}(\tilde{x})}{d\tilde{x}} = -\frac{1-\nu}{3-2\nu}\mathrm{CPV}\int_{-1}^{1}\frac{1}{\tilde{x}-\tilde{s}}\,d\tilde{s} + \int_{-1}^{1}\tilde{N}(\tilde{x}-\tilde{s})d\tilde{s}$$
$$= -\frac{1-\nu}{3-2\nu}\log\left(\frac{1+\tilde{x}}{1-\tilde{x}}\right) + \int_{-1}^{1}\tilde{N}(\tilde{x}-\tilde{s})d\tilde{s}, \quad |\tilde{x}| < 1 \qquad (71)$$

and hence

$$\frac{\pi\mu p_0}{b}\tilde{k}(\tilde{x}) = -\frac{1-\nu}{3-2\nu}[(1+\tilde{x})\log(1+\tilde{x}) + (1-\tilde{x})\log(1-\tilde{x})] + G(\tilde{x}) + C, \quad |\tilde{x}| < 1 \qquad (72)$$

with $G(\tilde{x}) = \int_{-1}^{\tilde{x}}\int_{-1}^{1}\tilde{N}(\tilde{t}-\tilde{s})d\tilde{s}d\tilde{t}$ and C an arbitrary constant which reflects the fact that the displacements within a (2D) half-plane can only be determined up to a rigid body motion.

Results and discussion

We now proceed to the discussion of the results obtained for the two indentation problems. In what follows, we investigate the effect of the ratio ℓ/b (normalized indent size) and the Poisson's ratio ν on the contact pressure distribution, the contact width, and the average pressure.

Figure 6 presents details of the pressure distribution characteristics below the cylindrical indentor. It is observed that the cylindrical indentor suggests a pressure distribution that depends monotonically on the ratio ℓ/b. Moreover, for increasing ratios ℓ/b, the pressure below the indentor increases significantly. In fact, as $\ell/b \to \infty$, the pressure tends to the limit $\sqrt{3-2\nu}p_{clas}(x)$. On the other hand, as $\ell/b \to 0$, we recover the classical elliptical pressure distribution. A qualitatively similar behavior is observed for the case of the wedge indentor in Figure 7. The effect of the ratio ℓ/b upon the pressure ratio distribution becomes more significant as we approach the sharp tip of the indentor $(x \to 0)$ where both solutions exhibit logarithmic-type singularities.

One of the most important information that one can obtain from indentation experiments is the indentation area (which essentially reduces to a contact width in the 2D case presented here) and the average pressure as

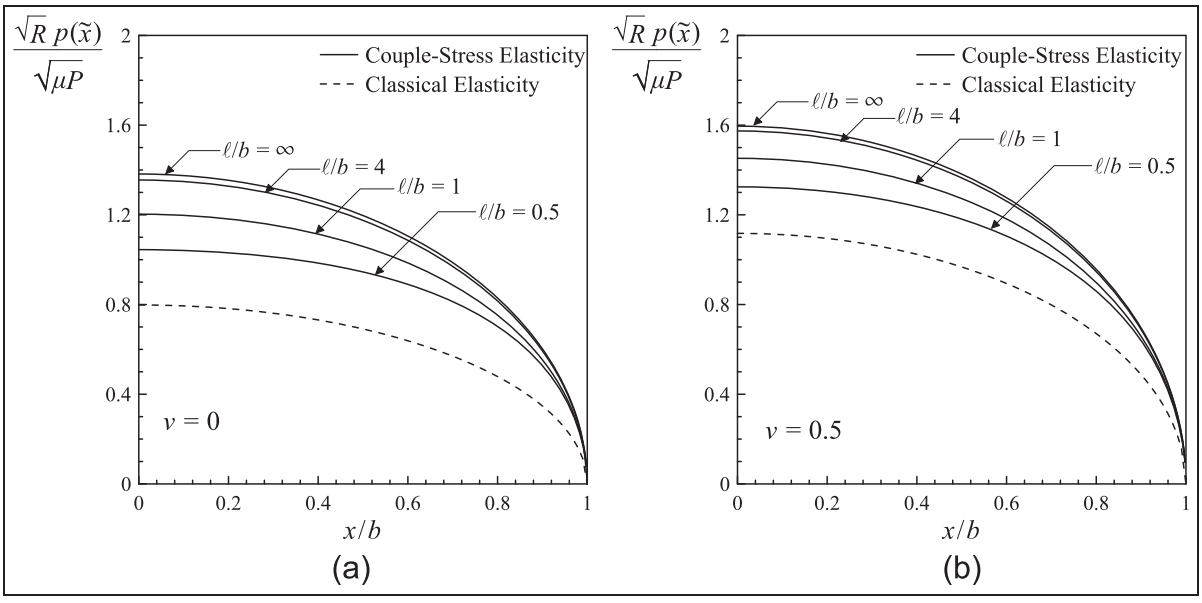

Figure 6. Distribution of the pressure below the cylindrical indentor with respect to the normalized distance x/b for various ratios ℓ/b. Results are shown for Poisson's ratios $\nu = 0$ and 0.5.

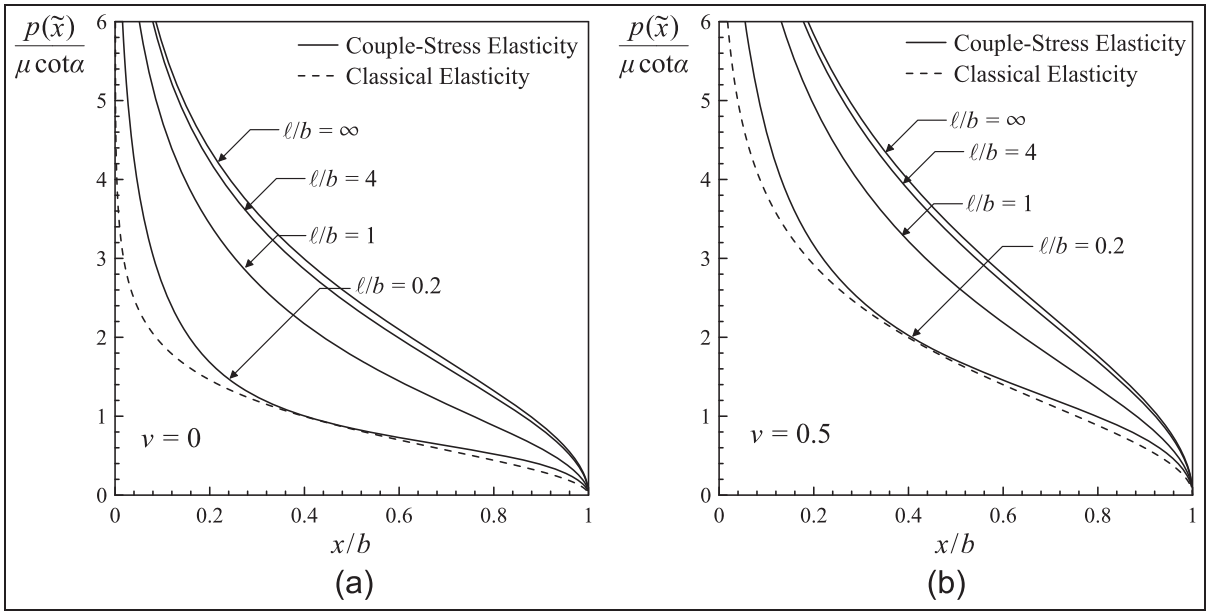

Figure 7. Distribution of the pressure below the wedge indentor with respect to the normalized distance x/b for different ratios ℓ/b. Results are shown for Poisson's ratios $\nu = 0$ and 0.5.

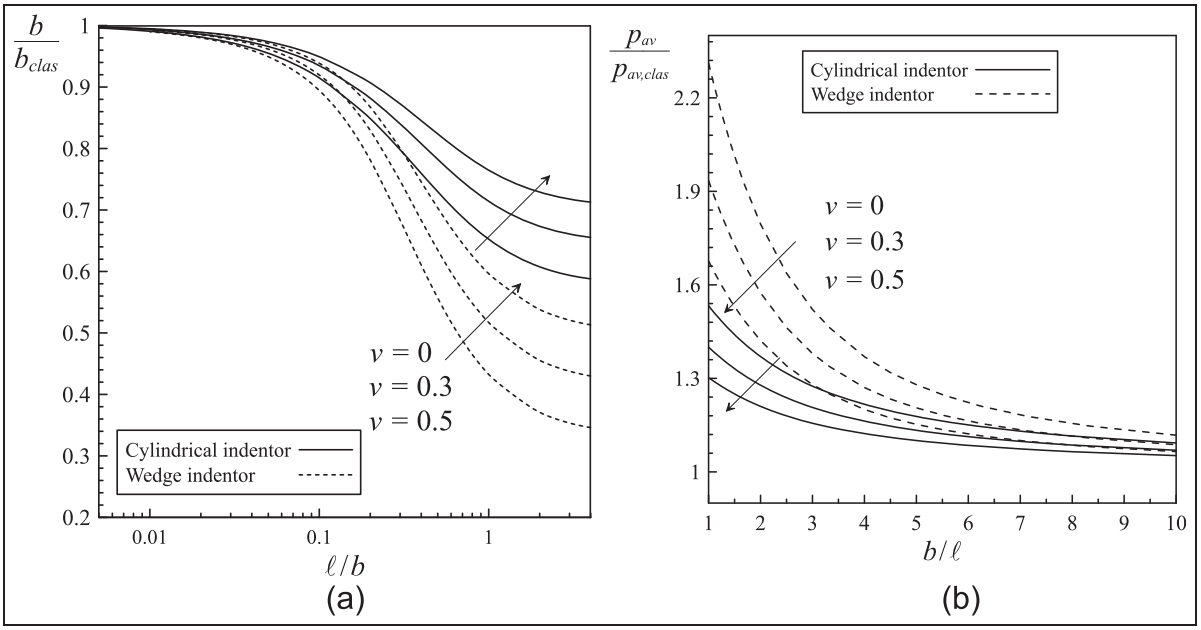

Figure 8. (a) Dependence of the dimensionless contact radius b/b_{clas} on the ratio ℓ/b and Poisson's ratio ν. (b) Dependence of the dimensionless average pressure $p_{av}/p_{av,clas}$ on the ratio b/ℓ and Poisson's ratio ν. Results are shown for the cylindrical and wedge indentors.

a function of the ratio ℓ/b (indent size). To this purpose, the half-contact width b is normalized with the corresponding half-contact width b_{clas} in classical elasticity. Note that $b_{clas} = (4(1-\nu^2)PR/(\pi E))^{1/2}$ (see, e.g., Johnson[50]). In the same spirit, the average pressure $p_{av} \equiv P/(2b)$ is normalized with the corresponding $p_{av,clas}$. The results are shown for the two cases studied previously, that is, the cylindrical and the wedge indentors.

In Figure 8(a), the dependence of the normalized contact width b/b_{clas} is shown as a function of the ratio ℓ/b, for different values of the Poisson's ratio ν. The contact width for both cylindrical and wedge indentors depends strongly on the ratio ℓ/b. Indeed, it is observed that for increasing ℓ/b, the measured contact width b decreases significantly. The qualitative dependence of the contact width upon ℓ/b is the same for both the cylindrical and wedge indentors. For $\ell/b > 2$, a plateau

is attained and no effect of the ratio ℓ/b upon the contact width is further observed. It should be emphasized that due to the characteristic dependence of the contact width on the ratio ℓ/b, in practice, the experimental results regarding the internal material length may be attained in the region $0.1 < \ell/b < 1$, where this dependence is more pronounced.

Next, Figure 8(b) illustrates the effect of the ratio b/ℓ on the normalized average pressure (hardness) $p_{av}/p_{av,\,clas}$. It is observed that when couple-stress effects are taken into account ($\ell \neq 0$), the hardness increases significantly compared to the classical prediction. For example, in the case of a wedge indentor and for a material with $\nu = 0.3$ and $b/\ell = 2$, a 57% increase is noted in the average contact pressure. As b/ℓ increases, the hardness decreases monotonically reaching the limit value of unity. Similar indentation size effects have been reported in the experiments performed by Han and Nikolov[8] during the elastic deformation of polymers and particularly of silicone. In their work, they showed that the indentation size effects are strongly related to the elastic and not merely to the plastic deformation as it is reported for the size-dependent deformation of metallic materials. In fact, indentation experiments with a Berkovich indentor carried out on heterochain polymers, such as polycarbonate (PC), epoxy, polyethylene terephthalate (PET), and polyamide 66 or nylon66 (PP66), showed an increased hardness with decreasing indentation depths, an experimental result which is qualitatively very similar to our p_{a_v} versus b relationship presented in Figure 8(b). Furthermore, Han and Nikolov[8] reported that the depth at which the hardness starts to increase depends strongly, in the elastic deformation regime, on the type of the polymer under consideration. In particular, they reported that the hardness at small indentation depths (or small contact areas) can increase from 0% to as much as 300%. In accord, our analysis showed that depending on the Poisson ratio, a maximum increase of about 30%–55% for the cylindrical and an increase of about 65%–130% for the wedge indentor are attained for a contact area (length) twice the size of the characteristic material length ($b/\ell = 1$) (see Figure 8).

Despite the qualitative similarities of the wedge and the cylindrical indentors, the former is distinctively more sensitive to ℓ/b as compared to the latter. For experimental purposes, both cylindrical and wedge indentors may be used in order to extract the characteristic material length ℓ of the indented material (Figure 8), but from a practical perspective the use of a large wedge angle and material failure in the highly stressed region immediately below the wedge tip may limit the applicability of the present analysis. On the other hand, the cylindrical indentor, although less sensitive to the variations in ℓ/b, is not susceptible to these drawbacks and may in reality be the best geometry to investigate the effect of material length scale on the behavior of a microstructured elastic material.

In closing, we present some results regarding the case of rigid punch generating uniform pressure over a strip of width $2b$ along the surface of the half-plane. Figure 9 illustrates the variation of the punch profile for various microstructural ratios ℓ/b. It is observed that for increasing ratios ℓ/b, the profile of the punch becomes more blunted exhibiting, thus a decreased curvature compared to the classical profile. The classical profile is reported to be[57]

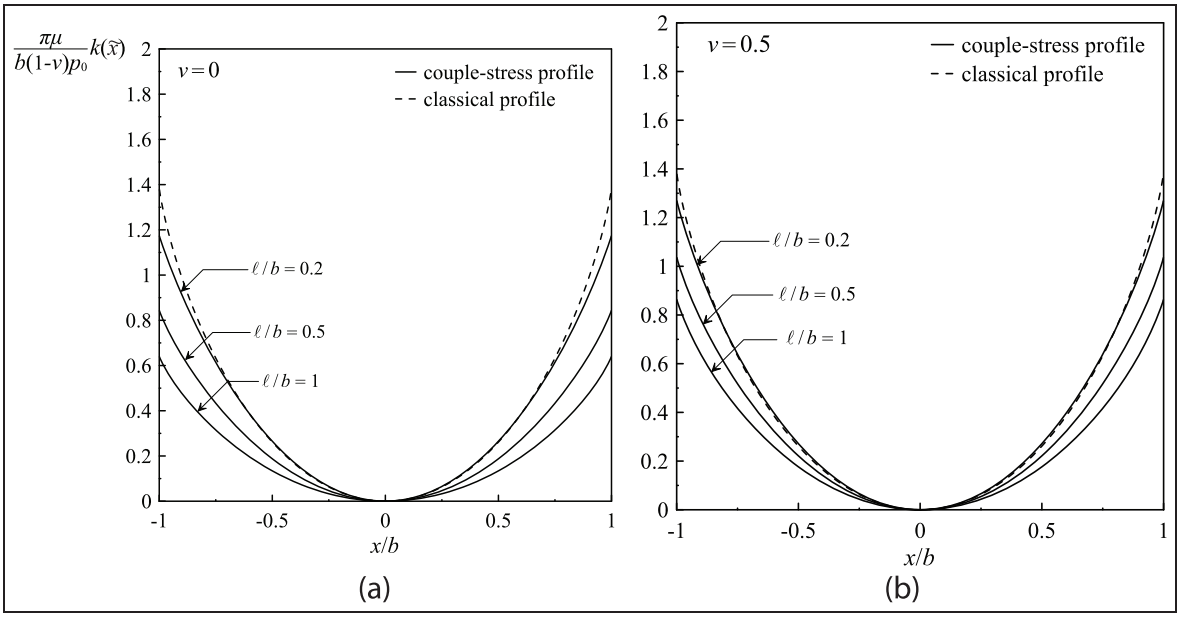

Figure 9. Profiles of the rigid punch producing a constant pressure distribution for different ratios ℓ/b. Results are shown for Poisson's ratios $\nu = 0$ and 0.5.

$$\tilde{k}_{class}(\tilde{x}) = \frac{b(1-\nu)p_0}{\pi\mu}$$
$$[(1+\tilde{x})\log(1+\tilde{x}) + (1-\tilde{x})\log(1-\tilde{x})] + C, \quad |\tilde{x}| \leqslant 1 \tag{73}$$

Note that the classical elasticity solution for the present normalization is independent of the Poisson's ratio effect, while the solution of the couple-stress elasticity retains the dependence on ν.

Conclusion

In this study, the half-plane Green's functions have been derived within the framework of the generalized continuum theory of couple-stress elasticity. This theory introduces a characteristic material length in order to describe the pertinent scale effects that emerge from the underlying microstructure. The Green's function is used for the formulation of two basic 2D plane strain contact problems—that is, the cylindrical and the wedge indentation problems—in terms of singular integral equations.

Our results exhibit significant departure from the predictions of classical elasticity. Regarding the concentrated load problem, we note that although the displacement components exhibit the same asymptotic behavior as in the classical theory, their detailed structure is quantitatively different in couple-stress elasticity. Moreover, in marked contrast to the classical theory, the rotation becomes bounded when calculated in the context of couple-stress theory. The departure from the classical elasticity is more significant near the point of the application of the load, where the rotation/strain gradients are more pronounced, while as we move further from the point of the application of the load the differences decay and the couple-stress solution approaches the classical.

Regarding the cylindrical and wedge indentation problems, it is shown that for increasing ratio ℓ/b the pressure below the indentor increases significantly compared to the classical elasticity predictions. Moreover, it is observed that as the characteristic material length ℓ increases, the contact width b decreases. In light of the above, the elastic indentation of microstructured solids, which introduces a more complex loading situation, may also act as a good alternative to common tests such as simple shear and pure bending in order to identify the characteristic material length and provide more accurate information closer to real-life conditions.

Declaration of conflicting interests

The author(s) declared no potential conflicts of interest with respect to the research, authorship, and/or publication of this article.

Funding

P.A.G. gratefully acknowledges support from the ERC advanced grant "Instabilities and nonlocal multiscale modeling of materials" under contract number FP7-PEOPLE-IDEAS-ERC-2013-AdG (2014-2019).

References

1. Stelmashenko NA, Walls MG, Brown LM, et al. Microindentations on W and Mo oriented single crystals: an STM study. *Acta Metall Mater* 1993; 41: 2855–2865.
2. Ma Q and Clarke DR. Size dependent hardness of silver single crystals. *J Mater Res* 1995; 10: 853–863.
3. Poole WJ, Ashby MF and Fleck NA. Micro-hardness of annealed and work-hardened copper polycrystals. *Scripta Mater* 1996; 34: 559–564.
4. Huber N, Nix WD and Gao H. Identification of elastic-plastic material parameters from pyramidal indentation of thin films. *Proc R Soc Lon Ser A* 2002; 458: 1593–1620.
5. Fleck NA, Muller GM, Ashby MF, et al. Strain gradient plasticity: theory and experiment. *Acta Metall Mater* 1994; 42: 475–487.
6. Larsson PL, Giannakopoulos AE, Söderlund E, et al. Analysis of Berkovich indentation. *Int J Solids Struct* 1996; 33: 221–248.
7. Fischer-Cripps AC. *Nanoindentation*. New York: Springer, 2004.
8. Han C-S and Nikolov S. Indentation size effects in polymers and related rotation gradients. *J Mater Res* 2007; 22: 1662–1672.
9. Nikolov S, Han CS and Raabe D. On the origin of size effects in small-strain elasticity of solid polymers. *Int J Solids* 2007; 44: 1582–1592.
10. Maranganti R and Sharma P. A novel atomistic approach to determine strain-gradient elasticity constants: tabulation and comparison for various metals, semiconductors, silica, polymers and the (Ir) relevance for nanotechnologies. *J Mech Phys Solids* 2007; 55: 1823–1852.
11. Pharr GM, Oliver WC and Brotzen FR. On the generality of the relationship among contact stiffness, contact area, and elastic modulus during indentation. *J Mater Res* 1992; 7: 613–617.
12. Chen X, Hutchinson JW and Evans AG. Simulation of the high temperature impression of thermal barrier coatings with columnar microstructure. *Acta Mater* 2004; 52: 565–571.
13. Stupkiewicz S. *Micromechanics of contact and interphase layers*. *Lecture notes in applied and computational mechanics*, vol. 30. Berlin: Springer, 2007.
14. Fleck NA and Zisis T. The erosion of EB-PVD thermal barrier coatings: the competition between mechanisms. *Wear* 2010; 268: 1214–1224.
15. Zisis T and Fleck NA. The elastic–plastic indentation response of a columnar thermal barrier coating. *Wear* 2010; 268: 443–454.
16. Tekoglu C and Onck PR. Size effect sin two dimensional Voronoi foams. A comparison between generalized continua and discrete models. *J Mech Phys Solids* 2008; 56: 3541–3564.

17. Muki R and Sternberg E. The influence of couple-stresses on singular stress concentrations in elastic solids. *Z Angew Math Phys* 1965; 16: 611–648.
18. Begley MR and Hutchinson JW. The mechanics of size-dependent indentation. *J Mech Phys Solids* 1998; 46: 2049–2068.
19. Nix WD and Gao H. Indentation size effects in crystalline materials: a law for strain gradient plasticity. *J Mech Phys Solids* 1998; 46: 411–425.
20. Shu JY and Fleck NA. The prediction of a size effect in microindentation. *Int J Solids Struct* 1998; 35: 1363–1383.
21. Wei Y and Hutchinson JW. Hardness trends in micron scale indentation. *J Mech Phys Solids* 2003; 51: 2037–2056.
22. Nielsen KL, Niordson CF and Hutchinson JW. Strain gradient effects in periodic flat punch indenting at small scales. *Int J Solids Struct* 2014; 51: 3549–3556.
23. Mindlin RD and Tiersten HF. Effects of couple-stresses in linear elasticity. *Arch Ration Mech An* 1962; 11: 415–448.
24. Mindlin RD. Influence of couple-stresses on stress concentrations. *Exp Mech* 1963; 3: 1–7.
25. Koiter W. Couple stresses in the theory of elasticity. Parts I and II. *Proc Nederl Akad Wetensch B* 1964; 67: 17–29.
26. Vardoulakis I and Sulem J. *Bifurcation analysis in geomechanics*. London: Blackie Academic & Professional (Chapman & Hall), 1995.
27. Huang Y, Chen JY, Guo TF, et al. Analytic and numerical studies on mode I and mode II fracture in elastic-plastic materials with strain gradient effects. *Int J Fracture* 1999; 100: 1–27.
28. Lubarda VA and Markenscoff X. Conservation integrals in couple stress elasticity. *J Mech Phys Solids* 2000; 48: 553–564.
29. Fleck NA and Hutchinson JW. A reformulation of strain gradient plasticity. *J Mech Phys Solids* 2001; 49: 2245–2271.
30. Georgiadis HG and Velgaki EG. High-frequency Rayleigh waves in materials with micro-structure and couple-stress effects. *Int J Solids Struct* 2003; 40: 2501–2520.
31. Grammenoudis P and Tsakmakis C. Finite element implementation of large deformation micropolar plasticity exhibiting isotropic and kinematic hardening effects. *Int J Numer Meth Eng* 2005; 62: 1691–1720.
32. Grentzelou CG and Georgiadis HG. Uniqueness for plane crack problems in dipolar gradient elasticity and in couple-stress elasticity. *Int J Solids Struct* 2005; 42: 6226–6244.
33. Radi E. Effects of characteristic material lengths on mode III crack propagation in couple stress elastic–plastic materials. *Int J Plasticity* 2007; 23: 1439–1456.
34. Gourgiotis PA and Georgiadis HG. An approach based on distributed dislocations and disclinations for crack problems in couple-stress elasticity. *Int J Solids Struct* 2008; 45: 5521–5539.
35. Dal Corso F and Willis J. Stability of strain-gradient plastic materials. *J Mech Phys Solids* 2011; 59: 1251–1267.
36. Gourgiotis PA and Piccolroaz A. Steady-state propagation of a mode II crack in couple stress elasticity. *Int J Fracture* 2014; 188: 119–145.
37. Triantafyllou A and Giannakopoulos AE. Derivation of strain gradient length via homogenization of heterogeneous elastic materials. *Mech Mater* 2013; 56: 23–37.
38. Zisis T, Gourgiotis PA, Baxevanakis KP, et al. Some basic contact problems in couple-stress elasticity. *Int J Solids Struct* 2014; 51: 2084–2095.
39. Chen JY, Huang Y and Ortiz M. Fracture analysis of cellular materials: a strain gradient model. *J Mech Phys Solids* 1998; 46: 789–828.
40. Bigoni D and Drugan WJ. Analytical derivation of Cosserat Moduli via homogenization of heterogeneous elastic materials. *ASME J Appl Mech* 2007; 74: 741–753.
41. Shodja HM, Zaheri A and Tehranchi A. Ab initio calculations of characteristic lengths of crystalline materials in first strain gradient elasticity. *Mech Mater* 2013; 61: 73–78.
42. Zhang X and Sharma P. Inclusions and inhomogeneities in strain gradient elasticity with couple stresses and related problems. *Int J Solids Struct* 2005; 42: 3833–3851.
43. Zhang X and Sharma P. Size dependency of strain in arbitrary shaped anisotropic embedded quantum dots due to nonlocal dispersive effects. *Phys Rev B* 2005; 72: 195345.
44. Lakes RS. Experimental methods for study of Cosserat elastic solids and other generalized elastic continua. In: *Continuum models for materials with microstructure*, 1995, pp.1–25, http://silver.neep.wisc.edu/~lakes/CossRv.pdf
45. Lakes RS. Strongly Cosserat elastic lattice and foam materials for enhanced toughness. *Cell Polym* 1993; 12: 17–30.
46. Green AE and Zerna W. *Theoretical elasticity*. Oxford: Oxford University Press, 1968.
47. Love AEH. *A treatise on the mathematical theory of elasticity*. New York: Cambridge University Press, 1952.
48. Fung YC. *Foundations of solid mechanics*. Englewood Cliffs, NJ: Prentice Hall, 1965.
49. Timoshenko SP and Goodier JN. *Theory of elasticity*. New York: McGraw-Hill, 1970.
50. Johnson K. *Contact mechanics*. Cambridge: Cambridge University Press, 1985.
51. Hills D and Nowell D. *Mechanics of fretting fatigue*. Dordrecht: Kluwer Academic Publishers, 1994.
52. Barber JR. *Elasticity: solid mechanics and its applications*, vol. 172. New York: Springer, 2010.
53. Georgiadis HG and Anagnostou DS. Problems of the Flamant–Boussinesq and Kelvin type in dipolar gradient elasticity. *J Elasticity* 2008; 90: 71–98.
54. Roos BW. *Analytic functions and distributions in physics and engineering*. New York: Wiley, 1969.
55. Sternberg E and Muki R. The effect of couple-stresses on the stress concentration around a crack. *Int J Solids Struct* 1967; 3: 69–95.
56. Ioakimidis NI. The numerical solution of crack problems in plane elasticity in the case of loading discontinuities. *Eng Fract Mech* 1980; 15: 709–716.
57. Hills DA, Nowell D and Sackfield A. *Mechanics of elastic contacts*. Oxford: Butterworth-Heinemann, 1993.